Numerical Simulation of HIWC Conditions with the Terminal Area Simulation System

Fred H. Proctor[1]
NASA Langley Research Center, Hampton, VA, 23681-2199

and

George F. Switzer[2]
Analytical Mechanics Associates, Inc., Hampton, VA, 23681-2199

Three-dimensional, numerical simulation of a mesoconvective system is conducted in order to better understand conditions associated with High Ice Water Content (HIWC) and its threat to aviation safety. Although peak local values of ice water content may occur early in the storm lifetime, large areas of high concentrations expand with time and persist even when the storm tops begin to warm. The storm canopy which contains HIWC, has low radar reflectivity factor and is fed by an ensemble of regenerating thermal pulses.

dBZ	=	decibels of radar reflectivity factor Z
D_{ic}	=	diameter ice crystals (*m*)
D_R	=	raindrop diameter
D_S	=	snow particle diameter
g	=	acceleration due to earth's gravity
$\|K_I\|^2$	=	dielectric factor for ice (=0.21)
$\|K_W\|^2$	=	dielectric factor for water (=0.93)
HIWC	=	High Ice Water Content
IMC	=	Instrumented Meteorological Conditions
IWC	=	ice water concentration (g/m^3)
M_R	=	mass water content for rain (kg/m^3)
$N(D_R)$	=	number of raindrops per unit diameter D_R per unit volume
$N(D_S)$	=	number of snow particles per unit diameter D_S per unit volume
N_{oH}	=	intercept value in hail/graupel particle size distribution (m^{-4})
t	=	time coordinate
TASS	=	Terminal Area Simulation System
T_C	=	temperature (Centigrade)
x,y	=	orthogonal space coordinates in lateral plane
V	=	horizontal component of velocity in y direction
z	=	vertical coordinate, elevation
Z	=	radar reflectivity factor
Z_R	=	radar reflectivity factor from rain
Z_S	=	radar reflectivity factor from snow
δ_S	=	snow particle density
δ_W	=	specific density of water

[1] Senior Research Scientist, Electromagnetics & Sensors Branch, MS 490, AIAA Senior Member.
[2] NASA Contractor, Electromagnetics & Sensors Branch, MS 490, AIAA Senior Member.

I. Introduction

HIGH concentrations of ice crystals associated with the upper-regions of large convective systems pose a threat to the safety of commuter and large-transport jet aircraft. The ingestion of high concentrations of ice crystals can cause uncommanded jet-engine power loss, such as roll-back and unstart, and in some cases result in engine damage.[1] These threat regions consist entirely, if not primarily, of ice crystals and differ from icing that is caused by accretion of supercooled water drops. In fact, reports of ice accretion during these events are rare.[2] These regions of dense ice-crystal concentrations are typically referred to as either High Ice Water Content[3] (HIWC) or High Altitude Ice Crystals[4,5] (HAIC), and have been linked with over a hundred incidents since the mid-1990s.[6] Incidents continue to occur with an average of about ten such incidents a year. So far, no injuries, fatalities, or loss of airframe have been reported due to pilots having been able to restart engines or gain lost power once they have descended into warmer regions or moved outside the threat area. Large areas that can expose jet engines to ice crystals for a duration of time (i.e. several minutes or more) seem more of a factor than brief encounters with local areas that have high concentrations. Thus, the HIWC threat is most associated with the large canopies of mesoconvective systems, rather than chance encounters with isolated short-lived thunderstorms. Detection of HIWC with the aircraft's weather radar is challenging, since the HIWC regions usually have low radar reflectivity and appear innocuous. In some cases HIWC incidents have occurred with only "black" (i.e. < 20 dBZ) being displayed from the aircraft's weather radar, although higher reflectivity may be detected at elevations below the event. According to Grzych and Mason,[7] satellites have detected a significant cold cloud-top region overlaying the location of most engine events. Other observations that may be associated with HIWC incidents include: presence of light turbulence (but rarely exceeding moderate), poor visibility (IMC), heavy rain below the freezing level, precipitation impacting the windshield, an indicated warming of the total air temperature (TAT) due to restrictions from accumulated ice in the TAT probe, St Elmo's fire, absence of hail, and cloud canopies that bulge above the tropopause. Environmental weather conditions leading to storms favorable for generating HIWC events are similar to those that produce mesoconvective systems and tropical storms. Only a few HIWC incidents have been reported with supercell convection and other strong continental storms, perhaps due to their association with higher levels of radar reflectivity factor that aircraft routinely detect and avoid. Most aircraft incidents have occurred from systems forming in deep moist environments with moderate to low convective instability.[7] Tropical and oceanic mesoconvective systems seem most likely for producing HIWC events that may pose a threat to aviation.[6]

Another threat from HIWC is that large concentrations of ice crystals can also cause blockage or restriction of the aircraft Pitot tubes, resulting in a loss of important information that may be critical for flight systems and pilot control. During NASA's DC-8 flight test in August of 2015, Pitot tube anomalies occurred with almost every flight, when HIWC was encountered and air temperatures were colder than -29C (see figure 1).

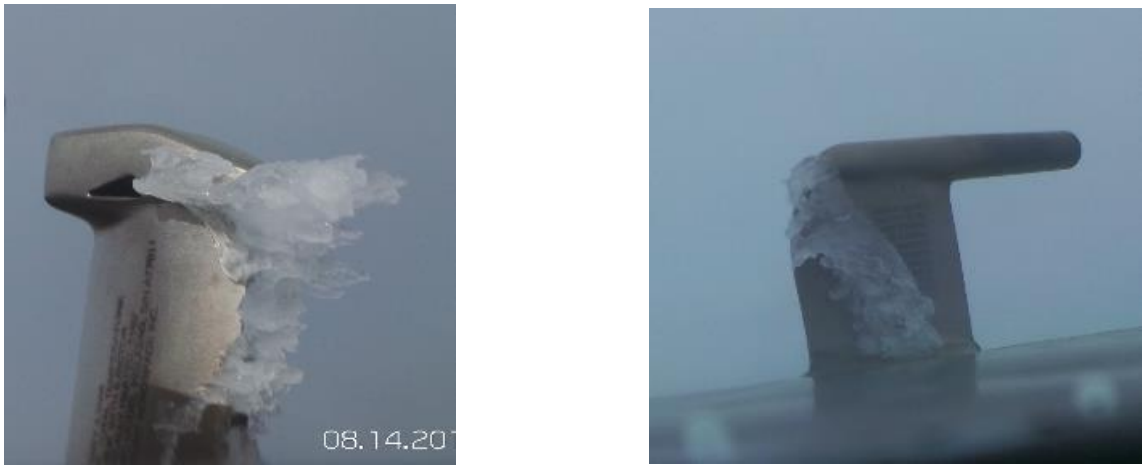

Figure 1. **Ice accumulation on TAT (left) and Pitot tube (right) sensors during encounter with HIWC conditions. Photographs taken from DC-8's cockpit during NASA's 2015 HIWC flight campaign.**

In order to better understand the characteristics of a HIWC event, a numerical simulation with a cloud-scale weather model is conducted. The case chosen for this simulation is from the International HAIC test campaign[8] that was conducted at Darwin, Australia in the winter of 2014.[5,9] The case is briefly described in Section II, followed by a description of the model and initial conditions in sections III and IV, and followed by an analysis of the simulation in section V. The case selected is thought typical of an oceanic HIWC system and relatively good measurements are

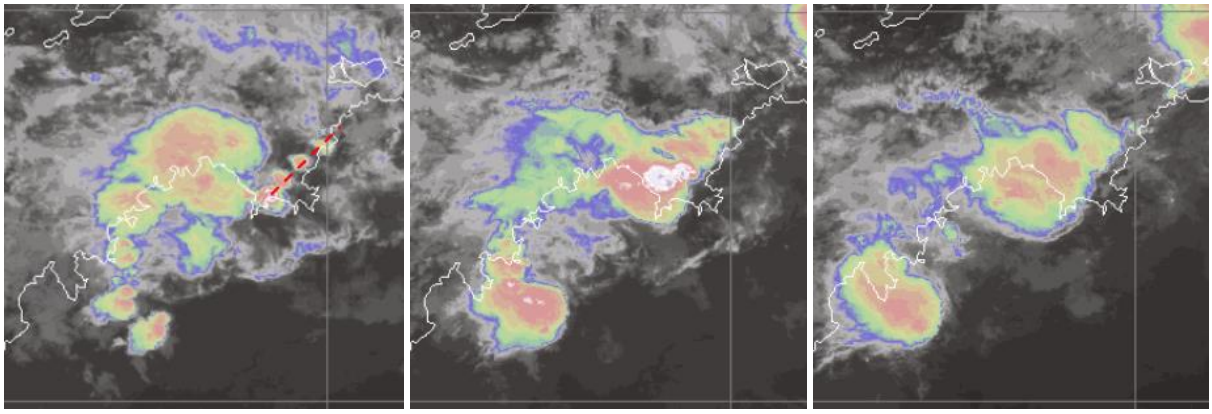

1830 UTC 2010 UTC 2240 UTC

***Figure 2*. Infrared satellite imagery showing cloud top temperatures of a mesoconvective system offshore of Northern Australia on 23 January 2014. Lat/Long of window is 122E-132E, 10S-20S. At 1830 UTC, the line of developing convection is located just to the east of a dying convective system (indicated by dashed line in left most figure). Imagery courtesy of P. Minnis and L. Nguyen, NASA Langley Satellite Team.**

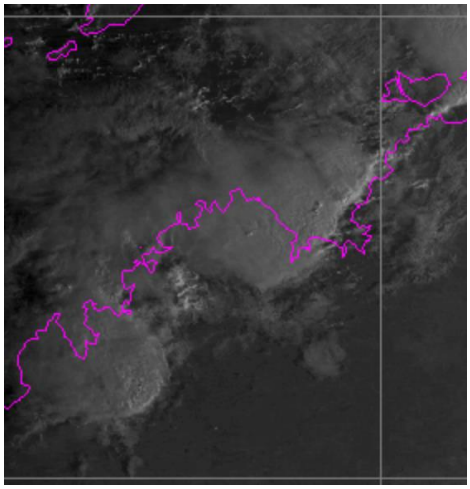

***Figure 3*. Same as figure 2, but for visible satellite imagery at 2210 UTC. Courtesy of P. Minnis and L. Nguyen, NASA Langley Satellite Team.**

available. Other cases from NASA's recent DC-8 flight campaign in 2015 are being investigated and will be reported later.

II. Darwin 23 January 2014 Case

Off the coast of Northwestern Australia, about 100 km southwest of Darwin, a line of convection developed nearly parallel to the coast, and was aided by old outflow boundaries from previous systems. A southwest-northeast line of at least four distinct cloud tops reached tropopause levels and began to expand in scale as shown in figure 2. The convection initially was spaced about 50 km apart, and the anvils merged and spread to the northwest. Coldest cloud tops were achieved several hours after convention began. The system appeared to weaken as indicated by warmer cloud tops, some 4 to 5 hours after convection began. The line of convection, as indicated by visible satellite imagery that was available following sunrise (figure 3) indicated little advancement of the line toward the southeast

An instrumented research aircraft probed the system at flight levels between 2100 and 2300 UTC and measured ice water concentrations frequently greater than 1-2 g/m^3 with peak values exceeding 3 g/m^3. Highest concentrations were measured near the end of the flight. During the last pass, ice water concentrations were measured above 2 g/m^3 persisting for three minutes and 1 g/m^3 or higher for five minutes. Unfortunately ground-based radar was located too far away to provide useful data of this system.

This mesoconvective system seems to typify many events associated with HIWC. Deep convection is triggered along a line and grows and merges into a larger mesoconvective system. Because the system persists for several hours, large canopies form and expand with time.

III. Model Description

The numerical simulations are performed with NASA's Terminal Areas Simulation System (TASS) which has the capability of simulating both liquid- and ice-phase cloud processes.[10,11,12,13,14,15] For treating cloud growth and precipitation development, TASS has over 60 bulk cloud microphysical submodels similar to those used by Lin et al.[16], and Rutledge and Hobbs[17]. The autoconversion of cloud droplets into rain is based on drop growth studies by Berry and Reinhardt,[18,19] and allows for differences in droplet size between continental and maritime locations.[10] The TASS model is three dimensional, and has prognostic equations for momentum, potential temperature, and pressure. Also it has continuity equations for water substance. The lateral boundaries can be open or cyclic. Initiation packages are available for triggering convective systems, turbulence, and aircraft wake vortices. TASS has a rich history of application to weather and wake vortex phenomenology, and has supported other NASA projects for the past 25 years.[20]

TASS divides the prediction of ice particles into three different categories: 1) ice crystal water — which represents small hexagonal ice crystals, 2) Snow — which represents larger precipitating ice particles, and 3) graupel (or hail) — which represents even larger more dense particles that are produced from freezing rain drops and riming snow particles. The ice crystal water is assumed to have a monodispersed particle size that is limited to diameters of about 200 *um*. The snow water assumes particles with an inverse exponential distribution that has an intercept that increases with decreasing temperature.[21] Hence, at colder temperatures, the assumed distributions will have smaller particles than at warmer temperatures. The graupel particles also assume an inverse exponential distribution, but with a smaller intercept and a larger particle density than snow. Several of the key parameters assumed for the particle distributions are shown in table 1.

Radar reflectivity factor is diagnosed from TASS based on the predicted water content and assumed particle distributions. The approach assumes Rayleigh scattering and is based on Smith et al.[22] For example, the radar reflectivity factor for rain based on Rayleigh scattering is:

$$\boldsymbol{Z_R = \int_0^\infty N(D_R)\, D_R^6 dD_R}$$

The radar reflectivity factor for ice particles consider the dielectric factors for ice and water and depend up whether the particle is undergoing either wet or dry growth. For example the contribution to radar reflectivity factor for "dry" snow adjust for the melted diameters is:

$$\boldsymbol{Z_S = \frac{|K_I|^2}{|K_W|^2}\ \frac{\delta_S^2}{\delta_w^2} \int_0^\infty N(D_S)\, D_S^6 dD_S}$$

Discrepancy between simulated and observed radar reflectivity factor is expected, since the above approach does not take into account the radar beam size, geometry, attenuation, and ground clutter.

The TASS model equations are discretized using quadratic-conservative fourth-order finite-differences in space for the calculation of momentum and pressure fields,[12] and the third-order upstream-biased Leonard scheme[23] is used to calculate the transport of potential temperature and water vapor. A Monotone Upstream-centered Scheme for Conservation Laws (MUSCL)-type scheme after van Leer[24,25] is used for the transport of water substance variables. The Klemp-Wilhelmson time-splitting scheme[26] is used for computational efficiency in which the higher-frequency terms are integrated by enforcing the CFL criteria to take into account sound wave propagation due to compressibility effects. The remaining terms are integrated using a larger time step that would be appropriate for anelastic and incompressible flows.[27] The Adams-Bashforth scheme is assumed for time differencing of momentum and pressure for both large and small time step approximations. The TASS model is programmed in FORTRAN and operates efficiently on massively-parallel computer architectures using Message Passing Interface (MPI) library calls.

T*able 1. Key parameters and relationships in TASS microphysics.*

Category	Size Distribution Intercept (m^{-4})	Particle Density ($kg\ m^{-3}$)	Comment
Cloud Water	Monodispersed	1000	Number of drops per volume is an input (=75 cm^{-3})
Rain	$2.25 \times 10^7\ M_R^{0.375}$	1000	Intercept increases with rainwater content, M_R ($kg\ m^{-3}$)
Cloud Ice	Monodispersed	Particle Mass (kg) = $0.1758\ D_{ic}^{2.2}$	Hexagonal plates Mostly < 200 um
Snow	$10^{(7.02\ -\ 0.475\ Tc)}$ for $4^oC > Tc > -40^oC$	100 if $Tc < -20^0C$ 100 +35/20 (Tc +20) if $Tc > -20^oC$	Intercept increases with decreasing temperature: graupel like snow
Hail/Graupel	N_{oH}	450	N_{oH} intercept used for graupel = $4 \times 10^5\ m^{-4}$)

Simulations with TASS are currently being used to 1) investigate and characterize regions of HIWC, 2) provide numerical data sets that can be used with radar simulation tools, and 3) contribute to the development of radar software for detecting regions of HIWC and other aviation hazards.

IV. Model Configuration and Initializations

A single sounding is used to initialize the simulation. The sounding for Darwin at 0000 UTC on the 24 January 2014 is the nearest in time and location, although the convective event occurs several hours earlier and approximately 100 *km* to the southwest. The sounding is modified for the observed surface temperature in vicinity of the event and is moistened through a deep layer as is frequently found in the vicinity of HIWC events.[7] The modified sounding is shown in figure 4. It has moderate convective instability, with a windshear vector between cloud base and 6-*km* elevation that is directed from 75 degrees (east-northeast).

In order to reduce the domain size while keeping adequate resolution needed for important convective scales, the domain is configured as 45 *km* wide x 112.5 *km* long, with cyclic boundary conditions assumed for left and right boundaries. The domain is rotated 15 degrees in the counter-clockwise direction so that the low level shear vector aligns orthogonal to the cyclic boundaries. The vertical depth of the domain is ~18.6 *km*. The computational domain is defined by 304x753x128 grid points with a grid size of 150 *m* in each direction.

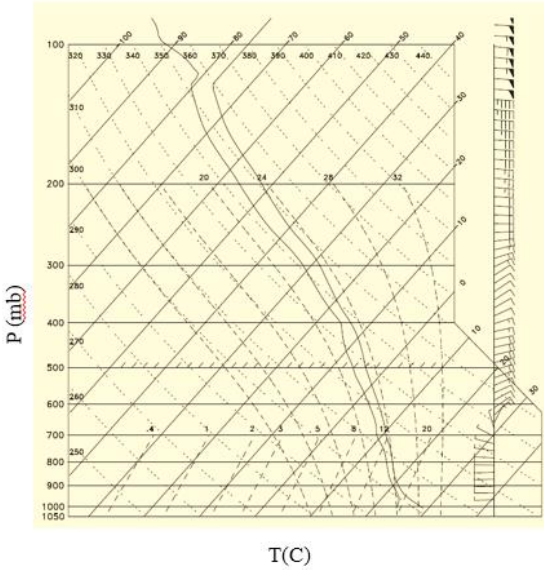

Figure 4. **Initialization sounding for Darwin case. Modified from sounding observed at Darwin Australia, at 0000 UTC, 24 January 2014.**

The ground surface is assumed flat to represent the ocean. Coastlines and topographical features are not incorporated into the simulation. Maritime cloud droplet concentrations are assumed at 75 droplets cm^{-3}. Other microphysical parameters as discussed in section II are not changed for this simulation.

V. Results

The simulation is initialized with a thermal impulse and executed for almost 4 hours of simulation time. Convection orients itself along a nearly stationary boundary and a cloud canopy expands northwestward like described in the observed case in section II. The simulated convective system is long lived, but begins to weaken shortly before four hours. An ensemble of regenerating updraft plumes, mostly originating along the forward line of the system, create ice particles that feed into the expanding upper-level canopy.

A summary of model comparison with available observed data for the Darwin case is show in table 2. The model simulation appears to catch the basic features of the storm, although the horizontal scale of the highest concentrations of ice is underpredicted. Also, there is slight difference in orientation of the convective line, which could be due to environmental difference not represented by the initial sounding,

A. Evolution of Simulated Fields

The tops of the convective system first reaches the tropopause around 85 *min*, with overall peaks reaching an elevation of 17.5 *km* at 120 *min*. Precipitation cooled outflows help regenerate other plumes along a forward line of heavy rain at the surface. Lighter rain spreads northwestward behind the line, with a few convective plumes developing under the canopy along the northwestern edge of the precipitation. The intensity of the system slowly weakens after 160 *min*, although convection remains vigorous and the system continues to expand in scale.

Table 2. Comparison between observed and simulated features for the Darwin case

Parameter	Observed	TASS
Orientation of convective line	southwest to northeast	west-southwest to east-northeast
Lifetime of system	5+ hours	4+ hours
Coldest cloud top temperature	-87ºC at 2019 UTC	-86ºC at t=165 minutes
Primary direction of canopy expansion	to west-northwest	to northwest
Line movement	nearly stationary	nearly stationary
Maximum IWC at flight level	3.5 $g\ m^{-3}$	3.5 $g\ m^{-3}$
Maximum scale of IWC greater than 1 $g\ m^{-3}$	65 *km*	40 *km*
Maximum scale of IWC greater than 2 $g\ m^{-3}$	40 *km*	10 *km*

The maximum ice water concentration above an elevation of 9 *km* is shown in figure 5. Peak local values of over 3.5 $g\ m^{-3}$ are achieved early in the system's lifetime; but early on, graupel contributes to a portion of the overall ice content. With time, the ice water concentrations expand in area and consist almost entirely of snow and cloud ice. As indicated in figure 5, peak ice water concentrations remain at or above 2.5 $g\ m^{-3}$ until 220 *min* (3*hrs*, 40 *min*) into the simulation. After which, the peak values begin to drop off rapidly. The values of ice water concentration are similar to what is expected from observations. In a review of deep-convective microphysics studies, Lawson et al.[2] reports measurements of ice water contents of up to 2.5 $g\ m^{-3}$. Higher values in excess of 3 $g\ m^{-3}$ have been measured during recent HIWC and HAIC programs.

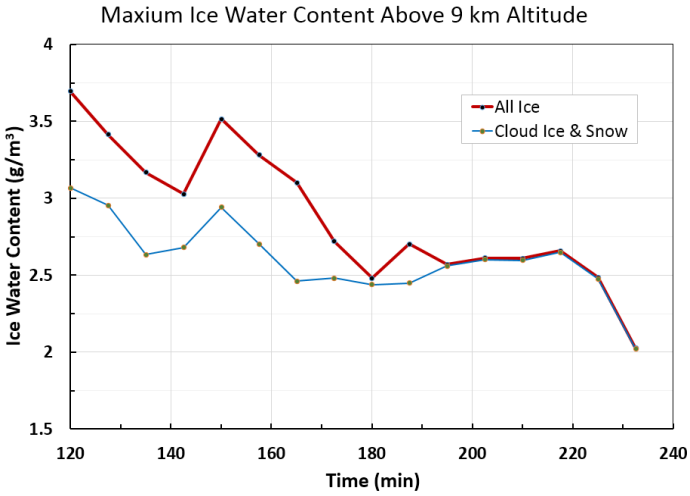

***Figure 5.* Maximum ice water above 9 *km* vs simulation time. The curve for "all ice" includes the contribution from ice crystals, snow, and graupel.**

Time evolution of the cloud top temperatures, as well as the radar reflectivity factor and cloud ice water fields at 10 *km* elevation are shown in figure 6. Horizontal cross-sections at this altitude are chosen since it will be near flight level and almost no liquid water can exist at temperatures colder than -30ºC. Three times are chosen. The first row is at *t*=120 *min* (2*hr*) and represents the early stage when the cloud tops are beginning to coalesce and fuse into a rapidly expanding canopy. The second row is at *t*=165 *min* (2*hr*: 45 *min*) representing the intense phase when cloud tops are very cold and peak ice water contents are large and beginning to expand over a significant area. The third column is at *t*=232.5 *min* (3*hr*: 52.5 *min*), represents the decay stage. At this last phase the cloud tops are extensive, but have become warmer (lower in elevation) and ice water concentrations have noticeably decreased. Only small areas of green (23-33 dBZ) are shown for the radar reflectivity fields at this level during the first two stages, and no green (or higher) is evident at the last stage. Note that most airborne weather radars would not display reflectivity below intensities indicated by green, so from a radar display, most of the area within the cloud canopy would appear innocuous in front of an aircraft traveling at that elevation. These levels of radar reflectivity are consistent with those found for deep oceanic convection by Heymsfield et al.[28] It is important to note from figure 6, that the highest ice water concentrations correlate with the locations of the overshooting tops and peak radar reflectivity during the early period of the storm system, but the coldest tops begin to warm and are displaced downshear from the highest regions of ice water content as the storm matures.

Vertical cross-sections of radar reflectivity factor taken orthogonal to the convective line are shown at the intense and decay stages in figure 7. Highest reflectivity is below the freezing level and near the surface, and decreases with elevation above five *km* elevation. This is consistent with radar measurements of deep oceanic convection, for example, as reported in Heymsfield et al.[28] Near the ground, figure 7 also shows heavy showers below the developing storm, this later changes to a large area of steady rain likely produced from melting snow.

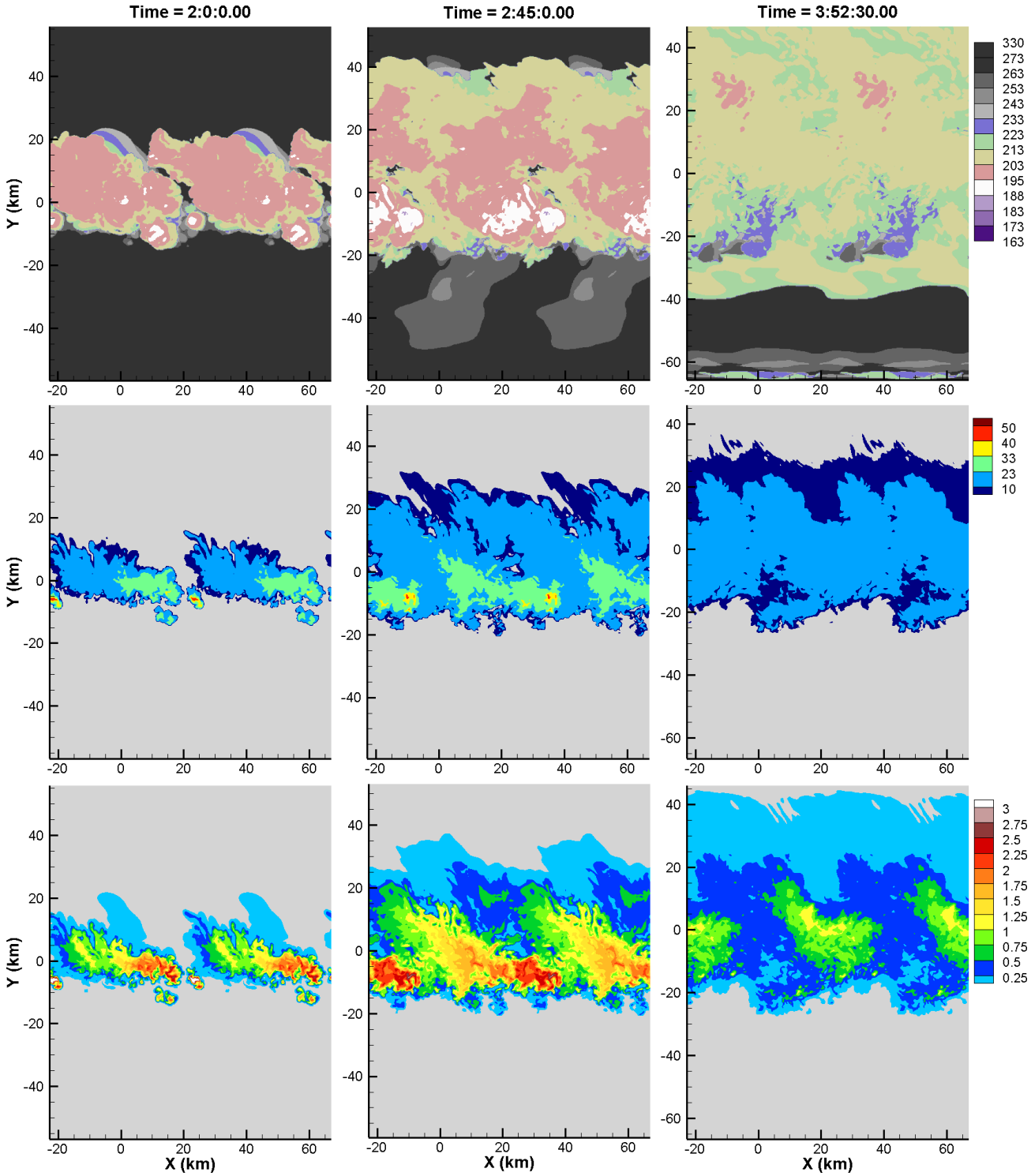

Figure 6. **Horizontal cross-sections of evolving fields at three different times from TASS. The same color scale for cloud top temperature in Kelvin (top row) is used as in figure 2 for observed satellite imagery. The second row is radar reflectivity factor at 10 *km* elevation, and the third row is ice water concentration *g* m^{-3}. The first column is at *t*=120 *min* (early stage), the second column is at *t*=165 *min* (intense phase), and the third column is at *t*=232.5 *min* during decay stage.**

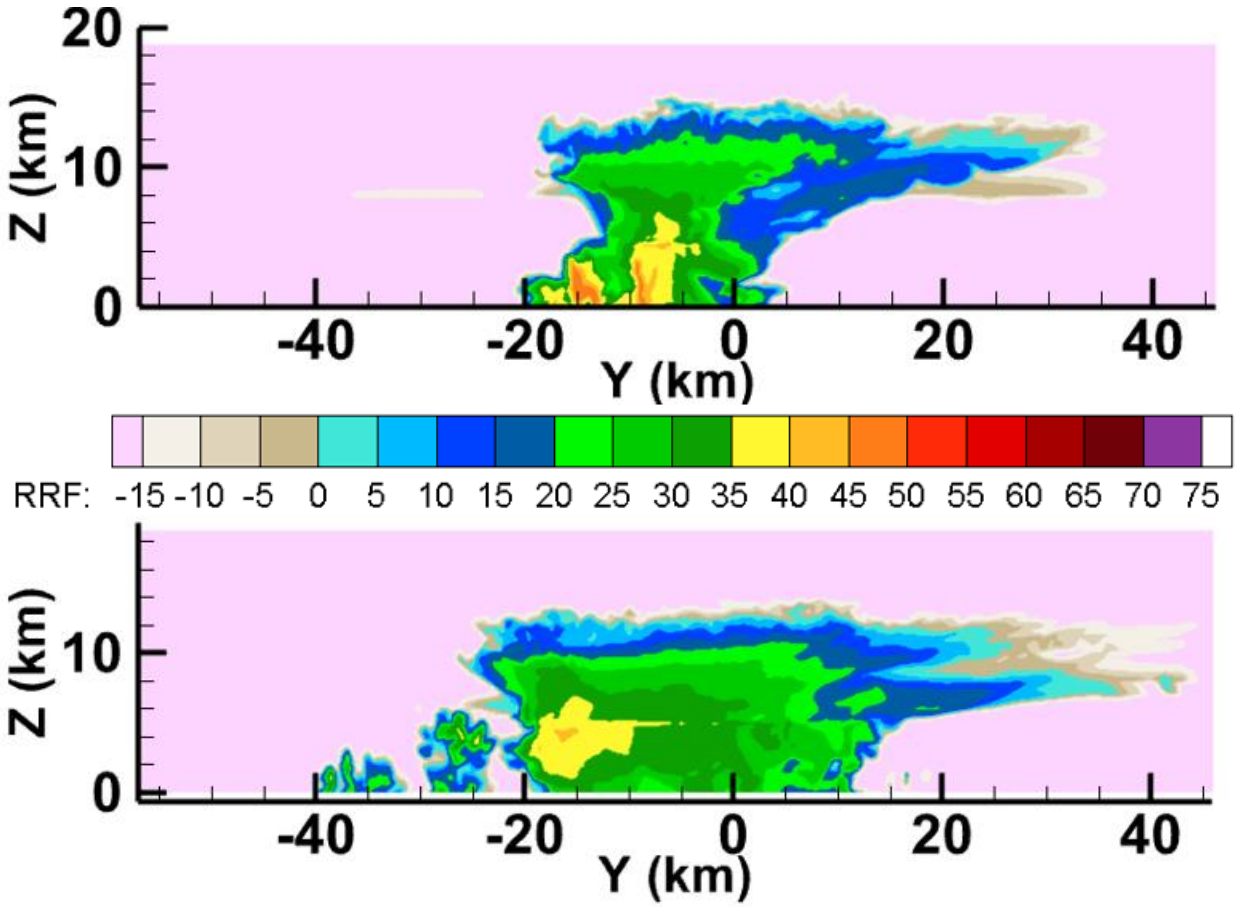

***Figure 7. V*ertical cross section orthogonal to convective line for radar reflectivity factor (dBZ). Top figure at *t*=165 *min* during intense phase, bottom at *t*=232.5 *min* during decay stage. The contours replicate the standard NEXRAD color pattern.**

B. Analysis of Mature Stage

A comparison of the simulated ice water field with other simulated fields is shown in figures 8-11 for the mature convective system. The horizontal cross sections again are taken at z = 10 *km*, near flight level. Note that ice water content exceeding 0.5 $g\ m^{-3}$ are nearly continuous along the line at y = -10 km, which is parallel to and just behind the front edge of the convective system. Ice water content greater than 1 $g\ m^{-3}$ extend approximated 45 *km* downshear (northwest) of the peak values that exceed 2.5 $g\ m^{-3}$. As shown in figure 8, radar reflectivity is mostly between 10-23 dBZ. Small areas of green (23dBZ -33 dBZ) are located within the regions of highest ice water concentration. From these results, it would appear difficult to avoid regions of high ice water content if the only available guide was the radar reflectivity at flight level.

The coldest tops (figure 9) have coalesced by this time and expanded ahead of the leading edge of the active convection, as well as expanded downshear beyond the model's lateral boundary. Coldest (and highest) tops at this time are displaced downshear from the regions of significant ice water concentration. A comparison of figures 8 and 9 show that the cold cloud top signatures are much larger than regions with either significant radar reflectivity or ice water content during this stage of development.

Simulated turbulence at flight levels are very light for the mature system (figure 10). This is not inconsistent with pilot briefings from actual HIWC incidents.[7] Flights through HIWC conditions during NASA's 2015 DC-8 HIWC campaign encountered turbulence ranging from light to nonexistent. Root-mean-square (rms) values of normal *g* load are TASS results processed according to methods described in references [29,30]. Since peak-g accelerations are about a factor of three greater than rms-*g* values, the peak g accelerations in figure 10 are less than 0.3 *g*.

The standard deviation (sigma) of the horizontal velocity component orthogonal to the convective line is shown in figure 11. The sigma values are several $m\ s^{-1}$ or less, but are greatest in the areas with larger IWC.

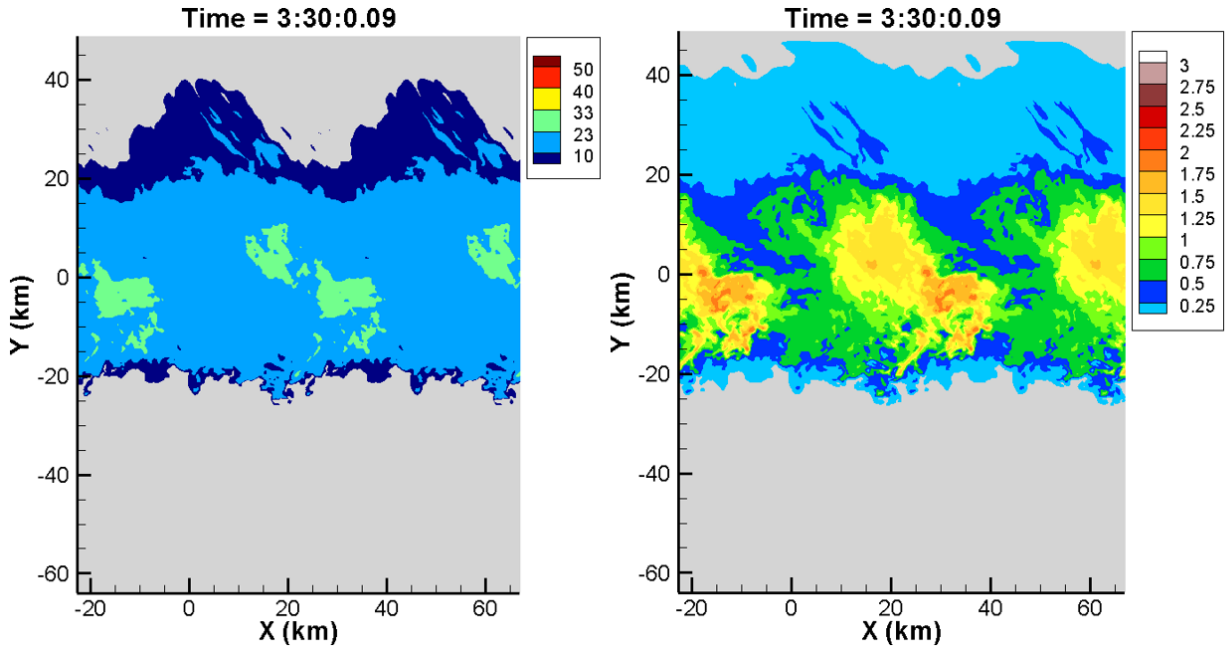

Figure 8. **Comparison of simulated radar reflectivity factor (left) with ice water concentration (right) at 10 *km* elevation for mature system (*t*=210 *min*). Radar reflectivity factor is in dBZ and IWC is in *g* m^{-3}.**

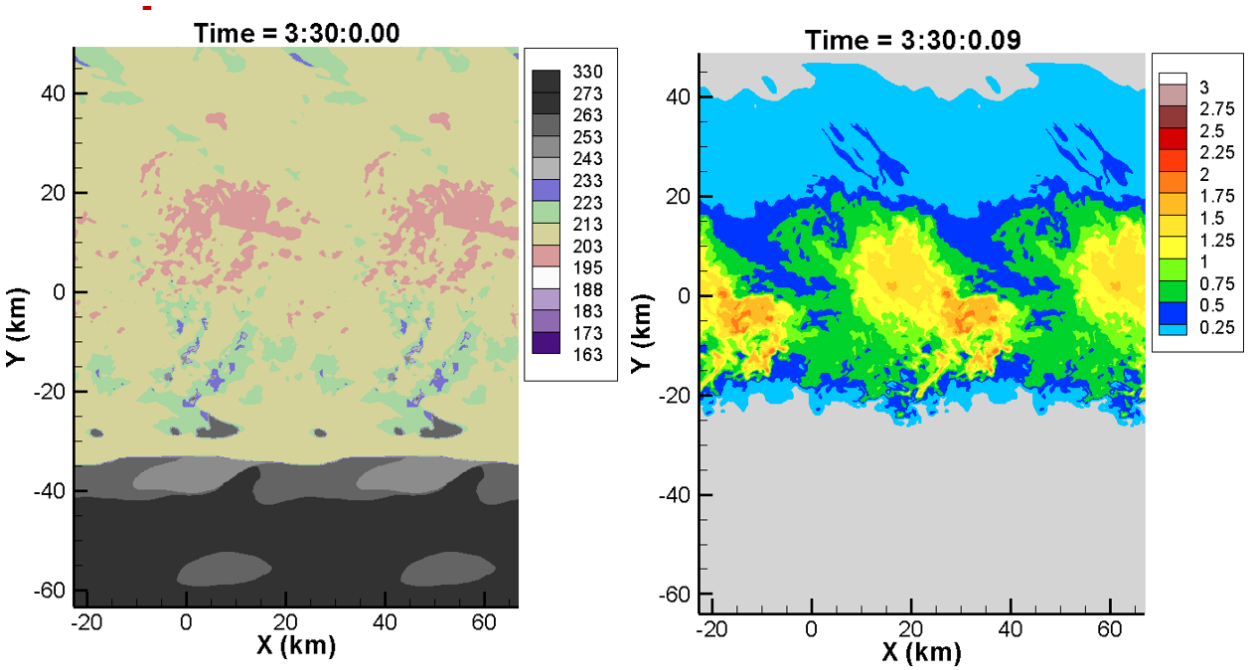

Figure 9. **Same as figure 8 but left figure is cloud top temperature in degrees Kelvin.**

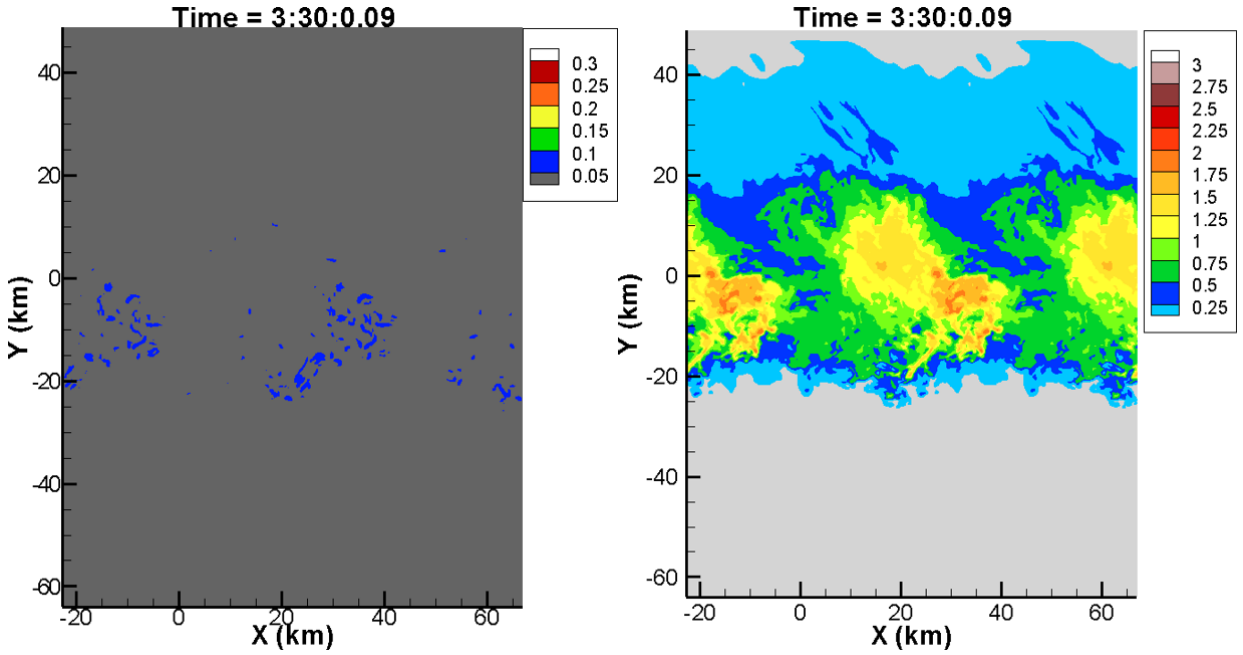

Figure 10. **Comparison of simulated turbulence intensity (left) assuming a B-757, and ice water concentration (right). Both plots are at 10 *km* elevation for mature system (*t*=210 *min*). Turbulence intensity expressed in rms-*g* accelerations and IWC is in *g* m^{-3}. Peak *g*-load accelerations are about three times greater than rms-*g*.**

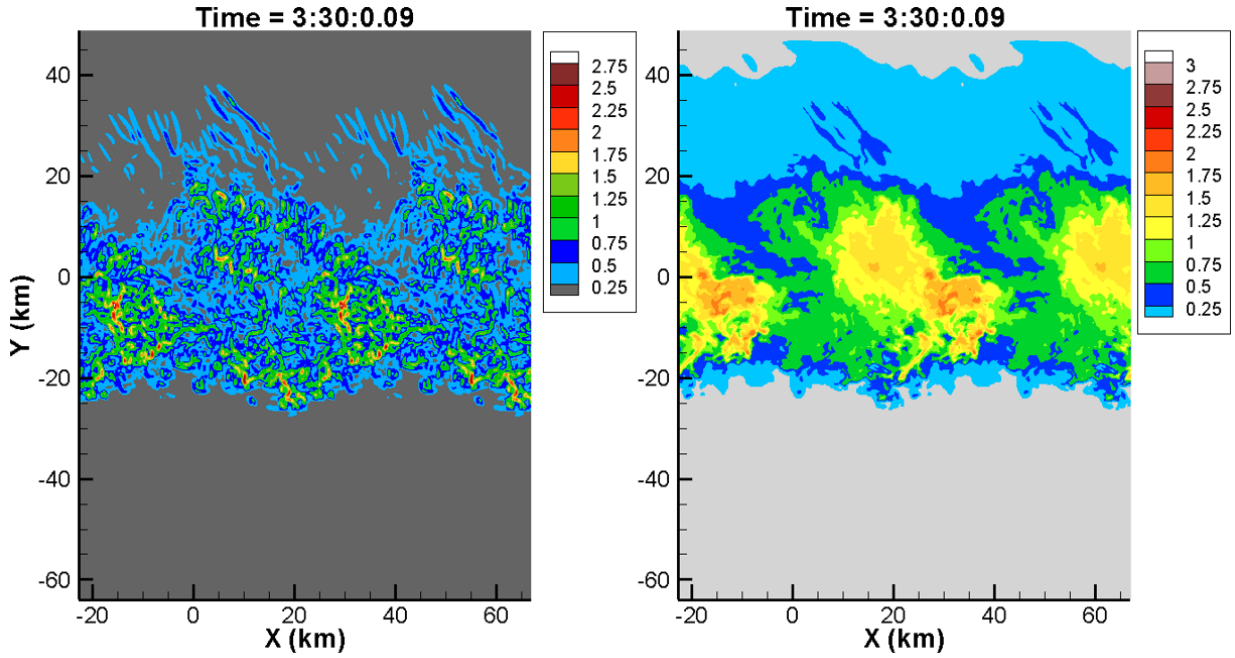

Figure 11. **Same as figure 10 but left figure is sigma V. The standard deviation is computed assuming a one *km* moving box. Units for sigma V are in *m/s*, and IWC is in *g* m^{-3}**

Figure 12 shows a vertical cross section of radar reflectivity factor and ice water concentration taken orthogonal to the convective line during the mature stage. Note that the highest ice water concentrations are near the forward area of the convective line. A region with 1 $g\ m^{-3}$ or greater is centered around 9-10 *km* elevation and extends along the *y*-coordinate for about 40 *km*. Ice water contents at elevations below this region likely decrease due to melting and sublimation. Also note that high radar reflectivity factors are not always found directly beneath regions of high ice water concentrations.

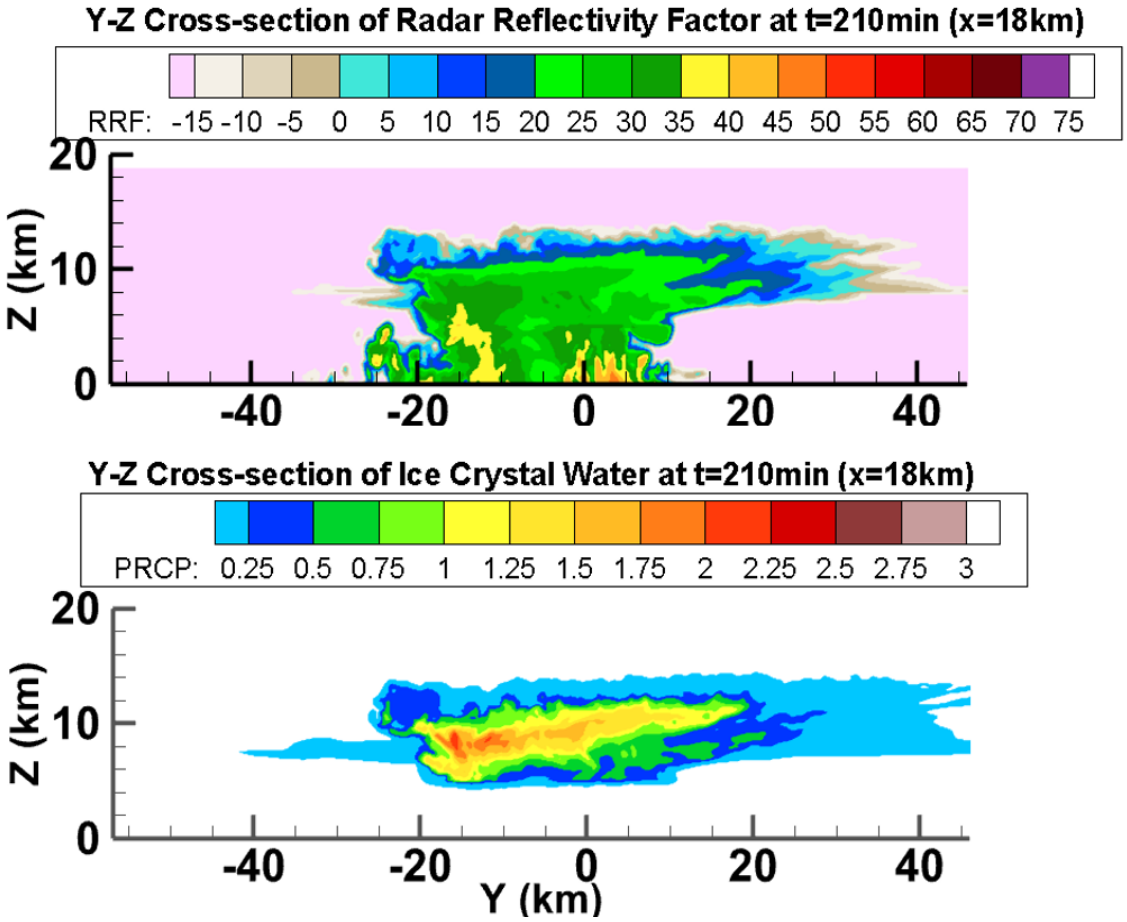

Figure 12. **Comparison of simulated radar reflectivity factor and ice water content for vertical cross-section orthogonal to line at during mature phase (*t*=210 *min*), units dBZ for radar reflectivity factor (top) and $g\ m^{-3}$ for ice water concentration (bottom).**

VI. Summary and Conclusions

A mesoscale convective line is simulated using the TASS model. The case represents a system that was observed during the HAIC program and was observed to contain high ice water concentrations for a sustained period along the flight track of a research aircraft. Many of the features that were observed and are known to occur from HIWC incidents were captured in the simulation. From these results, it would appear difficult to avoid regions of HIWC if the only available guide is the radar reflectivity at flight level.

Ice water concentrations exceeding 2 g/m^3 were found to persist beyond the most intense stages of the system.

The highest ice water concentrations correlate with the locations of the overshooting tops and peak radar reflectivity during the early period of the storm system, but this may not be true as the storm matures. During the decay phase of the convective system the coldest tops begin to warm and become displaced downshear from the highest regions of ice water content.

The modeling results were achieved without major updates to the TASS model or by utilizing parameters specifically changed or fine-tuned for HIWC type cases. The model can be robustly applied to all types of convection.

The modeled event has a structure very similar to that described and conceptualized by Houze et al.,[31,32] as shown in figure 13. From guidance provided by the case simulation, a region where the expected high ice water concentrations is to be expected is added to their conceptual model.

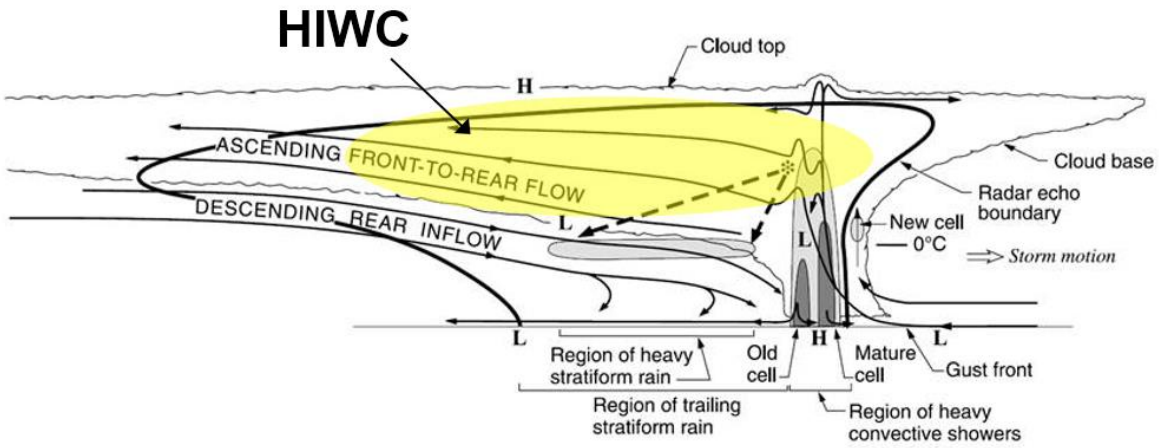

Figure 13. **Conceptual model of a convective line with trailing-stratiform precipitation viewed in a vertical cross section oriented perpendicular to the line. Intermediate and strong radar reflectivity is indicated by medium and dark shading, respectively. Dashed-line arrows indicate fallout trajectories of ice particles passing through the melting layer. HIWC denoted by yellow shading. Adapted from Houze et al. 1989].**

Acknowledgments

This research is sponsored by the Advanced Air Transport Technology Project of NASA's Advanced Air Vehicles Program. The authors would like to thank the project Co-PI's Steven Harrah of NASA Langley and Tom Ratvasky of NASA Glenn.

References

[1]Mason, J.G., Strapp, J.W., and Chow, P., "The Ice Particle Threat to Engines in Flight," AIAA 2006-206 doi:10.2514/6.2006-206.

[2]Lawson, R.P., Augus, L.J., and Heymsfield, A.J., "Cloud Particle Measurements in Thunderstorm Anvils and Possible Weather Threat to Aviation," *Journal of Aircraft*, Vol. *35*, No. 1, January-February 1998, pp. 113-121, doi: 10.2514/2.2268.

[3]Addy, H.E., Jr., and Veres, J.P., "An Overview of NASA Engine Ice-Crystal Icing," SAE International, 2011-38-0017, doi: 10.4271/2011-38-0017.

[4]Grandin, A., Merle, J-M., Weber, M., Strapp, J.W., Protat, A., and King, P. "AIRBUS Flight Tests in High Ice Water Content Regions," AIAA 2014-2753, doi:10.2514/6.2014-2753.

[5]Protat, A., and Rauniyar, S., Kumar, V.V., and Strapp, J.W., "Optimizing the Probability of Flying in High Ice Water Content Conditions in the Tropics Using a Regional-Scale Climatology of Convective Cell Properties," Journal of Applied Meteorology and Climatology, Vol. 53, November 2014, pp. 2438-2456, doi:10.1175/jamc-d-14-0002.1.

[6]Mason, J.G., and Grzych, M., "The Challenges Identifying Weather Associated with Jet Engine Ice Crystal Icing," SAE International 2011-38-0094, doi:10.4271/2011-38-0094.

[7]Grzych, M.L., and Mason, J.G., "Weather Conditions Associated with Jet Engine Power Loss and Damage due to Ingestion of Ice Particles: What we've Learned Through 2009," 14th Conference on Aviation, Range, and Aerospace Meteorology, American Meteorological Society, Paper Number 6.8, January 2010.

[8]Anonymous, "Publishable Summary," HAIC, URL: http://cordis.europa.eu/docs/results/314/314314/periodic2-haic-publishable-summary-version-october-2014.pdf

[9]Anonymous, "The 1st HAIC/HIWC International Field Campaign Started," HAIC Consortium, URL: http://www.haic.eu/the-1st-haichiwc-international-field-campaign-started/the-1st-haichiwc-international-field-campaign-started/

[10]Proctor, F.H., "The Terminal Area Simulation System, Volume 1: Theoretical Formulation," April 1987, NASA CR-4046.

[11]Proctor, F. H., and Bowles, R.L., "Three-Dimensional Simulation of the Denver 11 July 1988 Microburst-Producing Storm," *Meteorology and Atmospheric Physics*, Vol. 49, 1992, pp. 107-124, doi:10.1007/bf01025403.

[12]Proctor, F.H., "Numerical Simulation of Wake Vortices Measured During the Idaho Falls and Memphis Field Programs," 14th AIAA Applied Aerodynamic Conference, Proceedings, Part II, June 1996, AIAA 96-2496, pp. 943-960, doi:10.2514/6.1996-2496.

[13]Proctor, F.H., Hamilton, D.W., and Bowles, R.L., "Numerical Study of a Convective Turbulence Encounter," AIAA 2002-0944, doi:10.2514/6.2002-944.

[14]Ahmad, N., and Proctor, F.H., "Simulation of Benchmark Cases with the Terminal Area Simulation System," AIAA 2011-1005, doi:10.2514/6.2011-1005.

[15] Proctor, F.H., Ahmad, N.N., and Limon Duparcmeur, F.M., "Numerical Simulation of a Tornado Generating Supercell," AIAA 3012-0557, doi:10.2514/6.2012-557.

[16]Lin, Y-L., Farley, R.D., and Orville, H.D., "Bulk Parameterizations of the Snow Field in a Cloud Model," *Journal of Climate and Applied. Meteorology*, Vol. 32, 1983, pp. 1065-1092, doi:10.1175/1520-0450(1983)022%3C1065:bpotsf%3E2.0.co;2.

[17]Rutledge, S.A., and Hobbs, P.V., "The Mesoscale and Microscale Structure and Organization of Clouds and Precipitation. VIII: A Model for the "Seeder-Feeder" Process in Frontal Rainbands," *Journal of the Atmospheric Science*, Vol. 40, May, 1983, pp. 1185-1206 doi:10.1175/1520-0469(1983)040%3C1185:tmamsa%3E2.0.co;2.

[18]Berry, E.X., and Reinhardt, R.E., "An Analysis of Cloud Drop Growth by Collection. Part I: Double Distributions," *Journal of the. Atmospheric Science*, Vol. 31, October 1974, pp. 1814-1824, doi:10.1175/1520-0469(1974)031%3C1814:aaocdg%3E2.0.co;2.

[19]Berry, E.X., and Reinhardt, R.E., "An Analysis of Cloud Drop Growth by Collection. Part II: Single Initial Distributions," *Journal of the. Atmospheric Science*, Vol. 31, October 1974, pp. 1825-1831, doi:10.1175/1520-0469(1974)031%3C1825:aaocdg%3E2.0.co;2.

[20]Switzer, G. and Proctor, F., "Terminal Area Simulation System User's Guide – Version 10.0," January 2014, NASA TM-2014-218150.

[21]Woods, C.P., Stoelinga, M.T., and Locatelli, J.D., "Size Spectra of Snow Particles Measured in Wintertime Precipitation in the Pacific Northwest," J*ournal of the Atmospheric Science*, Vol. 65, January 2008, pp. 189- 205, doi:10.1175/2007jas2243.1.

[22]Smith, P.L., Jr., Myers, C.G., and Orville, H.D., "Radar Reflectivity Factor Calculations in Numerical Cloud Models using Bulk Parameterizations of Precipitation," *Journal of Applied Meteorology*, Vol. 14, September 1975, pp. 1156-1165, doi: 10.1175/1520-0450(1975)014%3C1156:rrfcin%3E2.0.co;2.

[23]Leonard, B.P., MacVean, M.K., and Lock, A.P., "The Flux-Integral Method for Multidimensional Convection and Diffusion," *Applied Mathematical Modeling*, Vol. 19, 1995, pp. 333-342, doi:10.1016/0307-904x(95)00017-e.

[24]van Leer, B., "Towards the Ultimate Conservative Difference Scheme: V, A Second-Order Sequel to Godunov's Method," *Journal of Computational Physics*, Vol. 32, 1979, pp. 101-136, doi:10.1016/0021-9991(79)90145-1.

[25]Ahmad, N.N., and Proctor, F.H., "Advection of Microphysical Scalars in Terminal Area Simulation System (TASS)," AIAA 2011-1004, doi:10.2514/6.2011-1004.

[26]Klemp, J. B., and Wilhelmson, R., "The Simulation of Three-Dimensional Convective Storm Dynamics," *Journal of the Atmospheric Sciences*, Vol. 35, June 1978, pp. 1070-1096, doi:10.1175/1520-0469(1978)035%3C1070:tsotdc%3E2.0.co;2.

[27]Switzer, G.F., "Validation Tests of TASS for Application to 3-D Vortex Simulations," October 1996, NASA CR-4756.

[28]Heymsfield, G.M., Tian, L., Heymsfield, A.J., Li, L., and Guimond, S., "Characteristics of Deep Tropical and Subtropical Convection from Nadir-Viewing High Altitude Airborne Radar," J*ournal of the Atmospheric Science*, Vol. 67, February 2010, pp. 285-308, doi:10.1175/2009jas3132.1.

[29]Proctor, F.H., Hamilton, D.W., and Bowles, R.L., "Numerical Study of a Convective Turbulence Encounter," AIAA 2002-0944, doi:10.2514/6.2002-944.

[30]Ahmad, N.N., and Proctor, F.H., "Large Eddy Simulations of Severe Convection Induced Turbulence". AIAA 2011-3201, doi:10.2514/6.2011-3201.

[31]Houze, R.A., Jr., Rutledge, S.A., Biggerstaff, M.I., and Smull, B.F., "Interpretation of Doppler Weather Radar Displays of Midlatitude Mesoscale Convective Systems," Bulletin of the American Meteorological Society, Vol 70, No. 6, June 1989, pp. 608-619, doi:10.1175/1520-0477(1989)070%3C0608:iodwrd%3E2.0.co;2.

[32]Houze, R.A., Jr., "Mesoscale Convective Systems, "Review of Geophysics, Vol. 42, RG4003, 2004, pp. 1-43, doi: 10.1029/2004RG000150.